Experimental Study on a Generic Side-View Mirror with Slotted Cylindrical Foot

W. Fu and Y. Li†

College of Mechanical & Electrical Engineering, Wenzhou University, Wenzhou, 325035, China

†*Corresponding Author Email: yli@wzu.edu.cn*

ABSTRACT

A simple model consisting of a mirror-housing and its cylindrical foot is applied to represent the automobile side-view mirror that causes unwanted aerodynamic noise and wind drag during high-speed driving. An additional slot is made on the solid foot to modify the flow around the mirror and thus reduce the side wall pressure fluctuation and aerodynamic drag. Flow fields and wall pressure fluctuations of these side-view mirror models have been investigated experimentally in a wind tunnel. The airflow rate through the slot varies with the changing of the slot area. Wall surface pressure sensors, particle image velocimetry (PIV), and six-component balance were applied to measure the acoustic and flow characteristics. The results demonstrated that, with the increase of slot airflow rate to 30%, the side wall pressure fluctuations were reduced by 5.1 dB and the drag coefficient decreased by 10.2%. The PIV measurements showed that the vortex cluster center behind the mirror was moved upward from the wall surface due to the slot airflow injection into the wake. The turbulent kinetic energy in the side-view mirror wake near the wall decreased with the increment of the airflow rate, reducing the side wall pressure fluctuations and thereby suppressing the noise generation.

Keywords: Automobile side-view mirror; Wall pressure fluctuation; Aerodynamic drag; Wind tunnel test; PIV.

NOMENCLATURE

W	width of the baseline mirror	U	mean x-streamwise velocity
b	width of the slot	U_∞	wind speed
D_1	diameter of the cylinder mirror housing	ΔLp	pressure fluctuation difference
D_2	diameter of the mirror foot	x	streamwise direction coordinate
H_1	height of the half-cylinder housing	y	transverse direction coordinate
H_2	height of the mirror foot	z	spanwise direction coordinate
H	height of the baseline mirror	$\tilde{u}_x$	x-streamwise fluctuating velocity
R	radius of the housing sphere	$\tilde{u}_y$	y-transverse fluctuating velocity
F	average drag force	$\tilde{u}_z$	z-spanwise fluctuating velocity
C_D	drag coefficient	δ	relative error
F_n	drag of each test	ρ	air density
p_{ref}	reference pressure	TKE	Turbulence Kinetic Energy
S	windward area of the mirror		
S_r	airflow rate through the slot		

1. INTRODUCTION

Automobile noise is composed mainly of engine noise, tire noise, and wind (aerodynamic) noise (Li *et al*. 2011). When a car runs at high speeds, aerodynamic noise becomes the dominant noise of the vehicle (Liu *et al.* 2018), in which the side-view mirror is one of the aerodynamic noise sources (Kim *et al*. 2011; Levy and Brancher 2013; Murad *et al.* 2013; Oettle and Sims-Williams 2017). The high-speed airflow separation from the mirror surface leads to severe pressure fluctuations on the side window (Zheng and Li 2012; He *et al*. 2020), which plays a significant role in the vehicle interior noise (Wang *et al*. 2010; Yang *et al.* 2014; Yao *et al*. 2018). Generally, the car interior noise level is considered a quality criterion in designing a comfortable automobile (Levy and Brancher 2015). In order to effectively suppress the aerodynamic noise caused by the side-view mirror, automotive

professionals worldwide have done a lot of theoretical analysis and application research.

Hold *et al.* (1999) and Siegert *et al.* (1999) used a generic side model consisting of a half-cylinder and a quarter of a sphere to predict aerodynamic sound sources and the aerodynamic noise. Lin *et al.* (2010) found that the noise mainly radiates from the side window surface where the vortices shed from the mirror impinge upon strongly. Thus, controlling the flow field near the side window is one of the measures to reduce the car aerodynamic noise. Kim and Han (2011) applied the technique of hot-wire and Laser Doppler Velocimetry (LDV) to measure the velocities in the mirror wake area. Kato (2012) proposed a numerical method to directly calculate the near-field and far-field noise around the side-view mirror. Different turbulence models, including Detached Eddy Simulation (DES) and Large Eddy Simulation (LES), were employed by Khalighi *et al.* (2012 and 2013) to analyze the unsteady flow around two different side-view mirrors.

Studies have demonstrated that the shape of a side-view mirror significantly influences the aerodynamic noise (Chen *et al.* 2014; Hu *et al.* 2020; Kim *et al.* 2020, 2021). So, reasonably improving the external geometry of the side-view mirror can effectively reduce the aerodynamic noise. Walker and Wei (2007) proposed that when the side-view mirror deflects by 30°, deemed the maximum realistic angle that could be used in production, the combining effect of buffeting and wind noise is the best. Tomac *et al.* (2011) delved into the interactions between the bluff body mirror geometry and its wake. The result showed that inappropriate geometrical design features of side-view mirrors could significantly exacerbate the flow-induced vibration levels of the mirror assembly. Wan and Ma (2017) applied the convex body structure of the dung beetle head to the original side-view mirror cover to reduce aerodynamic noise. The study showed that the improved side-view mirror could achieve a maximum noise reduction of 10 dB in the mid-high frequency region. Zhu and Liu (2018) suppressed noise by adding a cavity structure at the edge of the side-view mirror. The results showed that the maximum noise reduction of the optimized side-view mirror relative to the original model could reach 15.62%. Chen *et al.* (2018) showed that adding a serrated structure at the surface of the side-view mirror can effectively improve the wall pressure fluctuation in the mirror wake, thus effectively suppressing the noise generation. A study by Ye *et al.* (2021) found that applying a bionic shark fin structure to the side-view mirror shell can reduce the turbulence intensity in the wake region of the rearview mirror, and the maximum noise reduction could reach 7.3dB. Chode *et al.* (2021) used Computational Fluid Dynamics (CFD) to analyze the noise generated by the side-view mirrors with different aspect ratios and inclinations. The results showed that the maximum noise reduction of 4 dB was achieved when the side-view mirror was inclined by 32°.

From the literature mentioned above, much work on the side-view mirror noise attenuation was associated with the gap between the mirror body and the attachment plate, the width and height of the mirror foot, the inclination angle, etc. However, little attention is attracted to reducing the noise of the side-view mirror by modifying the solid foot. In addition, the vehicles are made according to the aerodynamic concept to prevent high-danger gas emissions and lower fuel consumption. Although the side mirrors are small, it still has a drag coefficient when driving at high speeds. The drag caused by the side-view mirrors generally accounts for 2-5% of the overall drag of the vehicle (Wan and Ma 2017). To reduce this drag force, the airflow over the side-view mirror needs to be low turbulence. Therefore, aerodynamic noise and wind drag are crucial parameters for the aerodynamic performance of commercial vehicles. So, the objective of this paper is to find a way to reduce the noise and drag forces by modifying the mirror foot instead of the mirror's external shape itself. A generic side-view mirror composed of half-cylinder housing and a solid cylindrical foot was considered a research item. Inspired by the work of Li *et al.* (2020) who applied a slotted rod to suppress vortex shedding, we considered making the cylindrical foot slotted so as to let the airflow pass through the slit into the mirror wake. Wind tunnel experiments were conducted to investigate the impacts of different mirror foot slotting airflow rates on the aerodynamic noise and drag force.

This paper is structured as follows: Section 2 focuses on the test model and the three wind tunnel experimental arrangements, including wall pressure fluctuation measurements, particle image velocimetry (PIV) flow field visualization, and aerodynamic drag measurements. Section 3 is the experimental results section, which mainly analyses and discusses the experimental results of different side-view mirror models. Finally, the conclusion is drawn in Section 4.

2. EXPERIMENTAL DETAILS

2.1 Mirror Models and Wind Tunnel Facility

A generic side-view mirror consisting of a mirror housing and its cylindrical foot is used as the baseline mirror model, as shown in Fig. 1. The width of the baseline model W is 90 mm, and the height H is 135 mm. The upper part is the mirror housing which contains a half-cylinder and a quarter of a sphere. The diameter of the cylinder (D_1) is 45 mm, equal to the sphere radius (R), and the height (H_1) is 60 mm. The lower part is the solid foot, with a diameter (D_2) of 25 mm and a height (H_2) of 30 mm. The coordinate origin of x, y, and z settled at the bottom center of the mirror foot. The size of the side-view mirror chosen in this paper is according to a flow blockage in a wind tunnel that is low enough not to affect the flow characteristics around the mirror.

Figure 2 shows the definitions of the mirror baseline and the other three models with different

slot sizes. For the slotted mirrors, the airflow rate S_r is defined as the ratio of the slotted area to the windward cross-sectional area of the mirror foot and is described as

$$S_r = \frac{15b}{25 \times 30} \tag{1}$$

where the slot height is 15 mm, and b is the width of the slot on foot. When b is 5 mm, 10 mm, and 15 mm, it corresponds to model ①, model ②, and model ③ with the corresponding airflow rates of S_r=10%, 20%, and 30%, respectively.
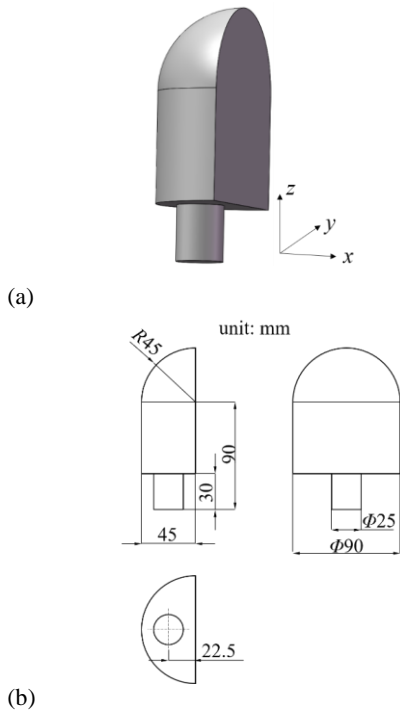

(a)

(b)

Fig. 1. Baseline side-view mirror model: (a) 3D diagram; (b) 2D diagram.

(a)

(b)
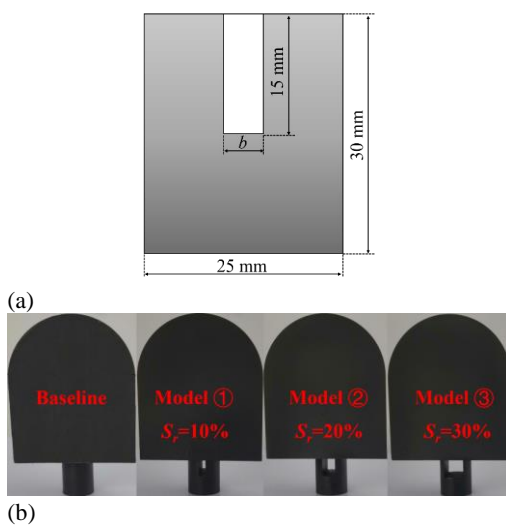
Fig. 2. Baseline model and the other three models with a slotted foot: (a) size of the slotted cylindrical foot; (b) physical models.

Experiment tests were carried out in the 0.5 m × 0.4 m test section acoustic wind tunnel at Wenzhou University. The wind tunnel is an open-circuit open-jet suction-type tunnel with low turbulence intensity (Niu *et al.* 2022). The side-view mirror models were installed on a flat plate connected to the wind tunnel nozzle at a downstream distance of 160 mm from the nozzle exit, as shown in Fig. 3. The flow blockage ratio of the side-view mirror is 4.7%, meeting the experimental requirement of less than 5% (Liu *et al.* 2018).

In this paper, the wind speed was set at U_∞=33.3 m/s, corresponding to the vehicle speed of 120 km/h. The main flow turbulence is about 0.15%. The Reynolds number Re_{D1} based on the mirror housing diameter D_1 is 2×10^5. At this wind speed, the thickness of the boundary layer is estimated to be 1.5 mm, far less than the height of the mirror foot. Thus, the effect of the boundary layer on the flow around the mirrors should not be significant (Porteous *et al.* 2019).
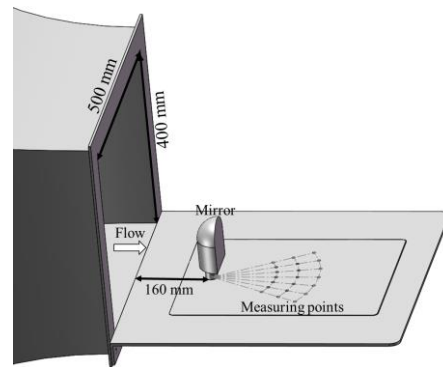

Fig. 3. Mirror test setup in wind tunnel.

2.2 Wall Pressure Measurements

Three rows of 21 pressure transducers (microphones) were flush-mounted on the flat plate to measure the wall pressure fluctuations in the wake of the side-view mirror. Fig.4 shows the arrangement of the pressure transducers on three circle arcs ($3R$, $4R$, and $5R$, R=45 mm) from the mirror foot center within ±30° with an increment of 10°.

The microphone sensors (BSWA MPA416) were connected to a preamplifier providing the power supply. The pressure fluctuations data were captured by a data acquisition card (NI-USB 6259) at a sampling rate of 51.2 kHz and analyzed using a block size of 4096, yielding a frequency resolution of about 12.5 Hz. The power spectral density (PSD) was calculated using Welch's method with a Hanning window and a block overlap of 50%. A total of 100 blocks were averaged for statistical confidence, and the uncertainty in the pressure fluctuation level was determined to be within 1% (the pressure fluctuation level difference between the repeated tests was less than 0.5 dB). The final results were given in dB as the sound pressure level (SPL) with a reference pressure of $p_{ref} = 2 \times 10^{-5}$ Pa.
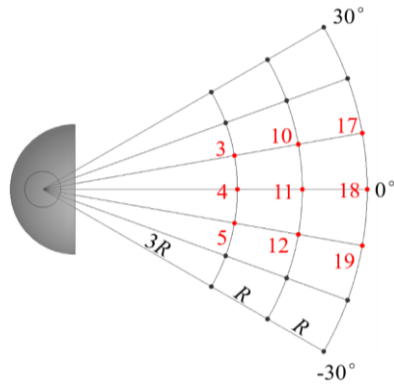
Fig. 4. Arrangement of the wall pressure transducers on the flat plate.

2.3 Particle Image Velocimetry (PIV)

2D-2C PIV experiments were conducted on three different plane sections of the side-view mirror to analyze the flow field variation in the wake. Flow fields on three planes, i.e., one longitudinal plane A at $y=0$, and the other plane B and plane C at $z=22.5$ mm and 60 mm, were investigated. The test frequency of the PIV is 5 Hz, and Figure 5 shows its installation schematic and wind tunnel setup.

The flow velocity data were acquired using the PIV system of SM3-5M200 with a New Wave Gemini Nd: YAG dual laser that emits laser pulses with a maximum energy of 120 mJ. A NIKON CCD camera with a resolution of 2,456 (pixels) $\times$ 2,672 (pixels) was set up perpendicularly to the laser sheet on the scan plane. The flow was seeded with a tracer particle of approximately 1 μm diameter, generated by burning Sulphur and saw powder. The laser light sheet thickness at the model area is about 1 mm. The measurement area of the PIV system is 350 mm~350 mm. When shooting the longitudinal section plane A, the laser ejector is located directly above the models, and the camera is installed at the vertical position. When the two cross-section planes (B and C) are needed, the laser ejector and camera positions exchange each other. A total of 400 PIV images were shot for each experimental configuration. Each image set was processed using a 32 (pixels) $\times$ 32 (pixels) cross-correlation area and a 50% $\times$ 50% overlap. The uncertainty of the instantaneous velocity measurements is estimated to be within 2%.

2.4 Six-component Balance Setup

The aerodynamic performances were measured using the six-component balance: ATI mini 45 Transducer, which has a compact, low-profile design with high capacity and a through-hole to allow passage of cables. The minimum resolution is 0.0625 N, and the measurement range is -580 N to + 580 N when the six-component balance is applied to measure drag force. Figure 6 shows the schematic diagram of the six-component balance installation, with the side-view mirror model fixed at the upper end of the balance and a 2 mm gap between the left and right sides of the balance and the baffle to detect the force of airflow on the side-view mirror.
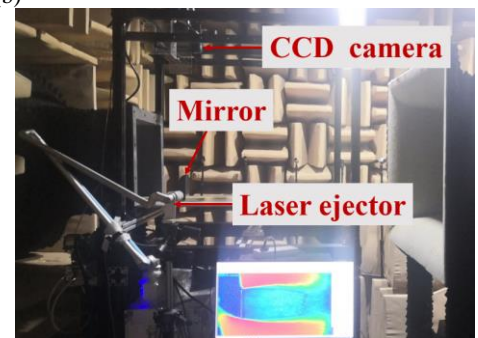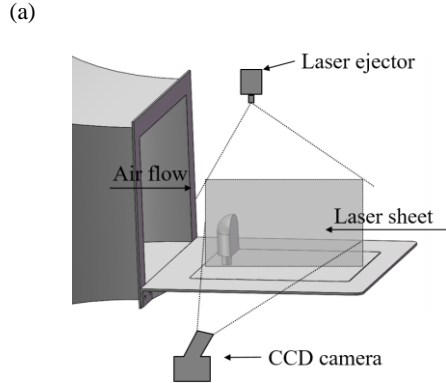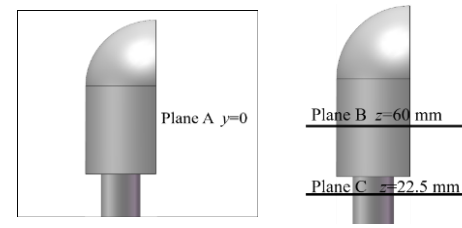

(a)

(b)

(c)

Fig. 5. PIV test layout: (a) three planes; (b) schematic diagram photographing cross-section; (c) wind tunnel setup.
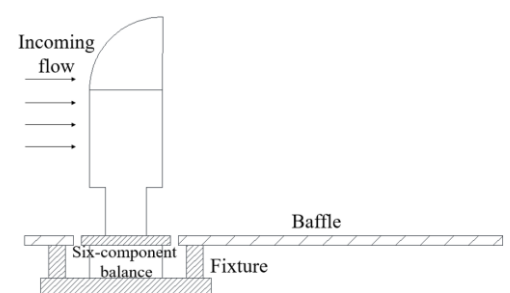

Fig. 6. Schematic diagram of the six-component balance setup.

3. EXPERIMENTAL RESULTS AND DISCUSSION

3.1 Wall Pressure Fluctuation

The wall pressure fluctuations measured in the experiments contain both the convective and acoustic parts. The latter is much smaller than the former (Caro *et al*. 2014; Dawi and Akkermans 2019), so the wall pressure fluctuations are approximately regarded as composing only the
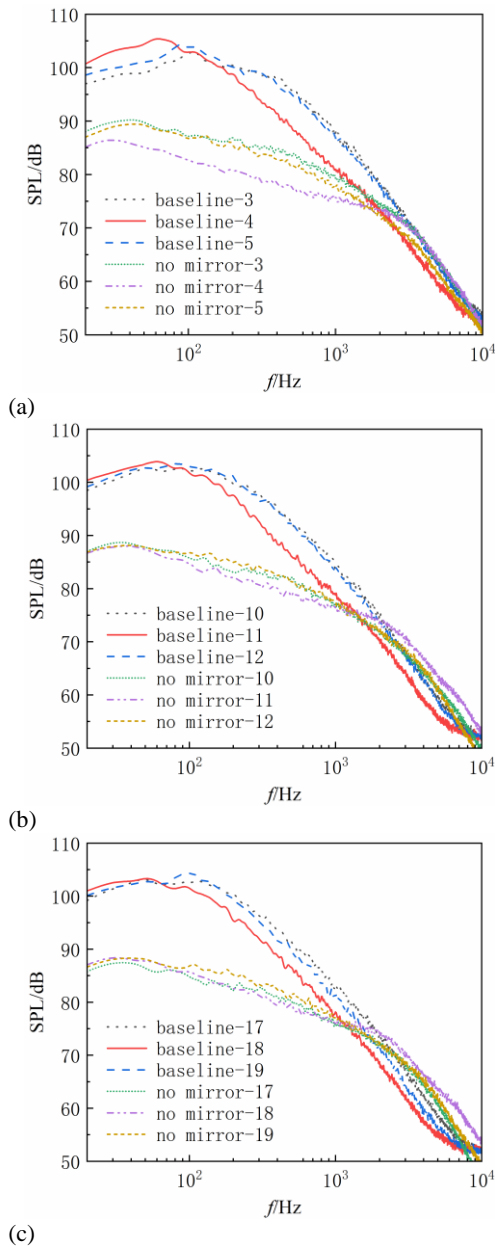
Fig. 7. Spectrum comparison of measuring points in the core area of the baseline mirror wake. (a) first row; (b) second row; (c) third row.

convective part. By checking all the 21 measuring points on the flat plate, we observe that the wall pressure fluctuations in the middle region of the side-view mirror wake (i.e. the area between -10° and +10°) are much greater than those of the monitoring points in other areas, which is in agreement with the statement by Chen *et al.* 2009. Therefore, the pressure spectrum is analyzed mainly at points 3, 4, 5, 10, 11, 12, 17, 18, and 19 on the flat plate in the wake core area.

Figure 7 shows the spectrum comparison of the wall pressure fluctuation of the nine measuring points in the core area of the baseline mirror wake. Also included is the pressure spectrum at each measuring point without any mirror. At the frequency region

between 20 Hz and 1 kHz, the background pressure is far lower than that of the side-view mirror models. The pressure fluctuation generated by the side-view mirror has broadband characteristics, and the energy mainly concentrates on the low-mid frequency range. Among these nine measuring points, the SPLs of the two points on both sides of the centerline are very close in the whole frequency band, mainly due to the flow symmetry. Therefore, the spectral analysis of wall pressure fluctuation at six points, including 3, 4, 10, 11, 17, and 18, is mainly conducted in the following. In addition, compared with those points 4, 11, and 18, the SPLs at points 3, 5, 10, 12, 17, and 19 are much higher, especially for frequencies above 60 Hz. As seen in Fig. 4, the former three points (4, 11, and 18) are on the centerline in the wake area of the mirror, whereas the latter six points are on the sideline 10° offside from the center. It indicates that the six points are in the region where the flow field is much more turbulent and has severe pressure fluctuations, which is understood since these measuring points are in the shear layers of the mirror foot.

Figure 8 shows the narrow-band spectrum comparison of these four mirror models at the six offside measuring points in the wake core area. Compared with the baseline mirror, all three slotted models have pressure reduction in broadband frequencies below 500 Hz, and the pressure reduction obtained increases with the airflow rate S_r increasing. The maximum pressure reduction achieved by model ① with $S_r=10\%$ is no more than 3 dB at all the measuring points. Model ② with $S_r=20\%$ can achieve the maximum reduction of nearly 10 dB within some frequency range at point 4 and more than 5 dB at the other five measuring points. With the airflow rate of $S_r=30\%$, model ③ has a maximum pressure reduction of more than 10 dB at measuring points 3, 4, and 10. In addition, we can observe that all three slotted models have a frequency hump between 50 and 60 Hz, indicating that some quasi-periodic pulsations may exist in these three flow fields.

Table 1 presents the average reduction of overall sound pressure level (OASPL) in different frequency ranges achieved by the three slotted models at the nine measuring points. Here ΔL_p represents the pressure fluctuation difference between the OASPL of the slotted models and the baseline mirror. It is the average variation in OASPL of the nine wall pressure fluctuations of the slotted model relative to the baseline. Negative values indicate pressure fluctuation reduction, while positive values mean pressure fluctuation increase. In the frequency range below 500 Hz, the average OASPL at the nine measuring points is reduced by 1.8 dB, 3.9 dB, and 5.1 dB for model ①, model ②, and model ③, respectively. In the frequency range of 20 Hz-10 kHz, the corresponding reduction of the OASPL is 1.5 dB, 3.3 dB, and 4.6 dB.

3.2 Mean Flow Field

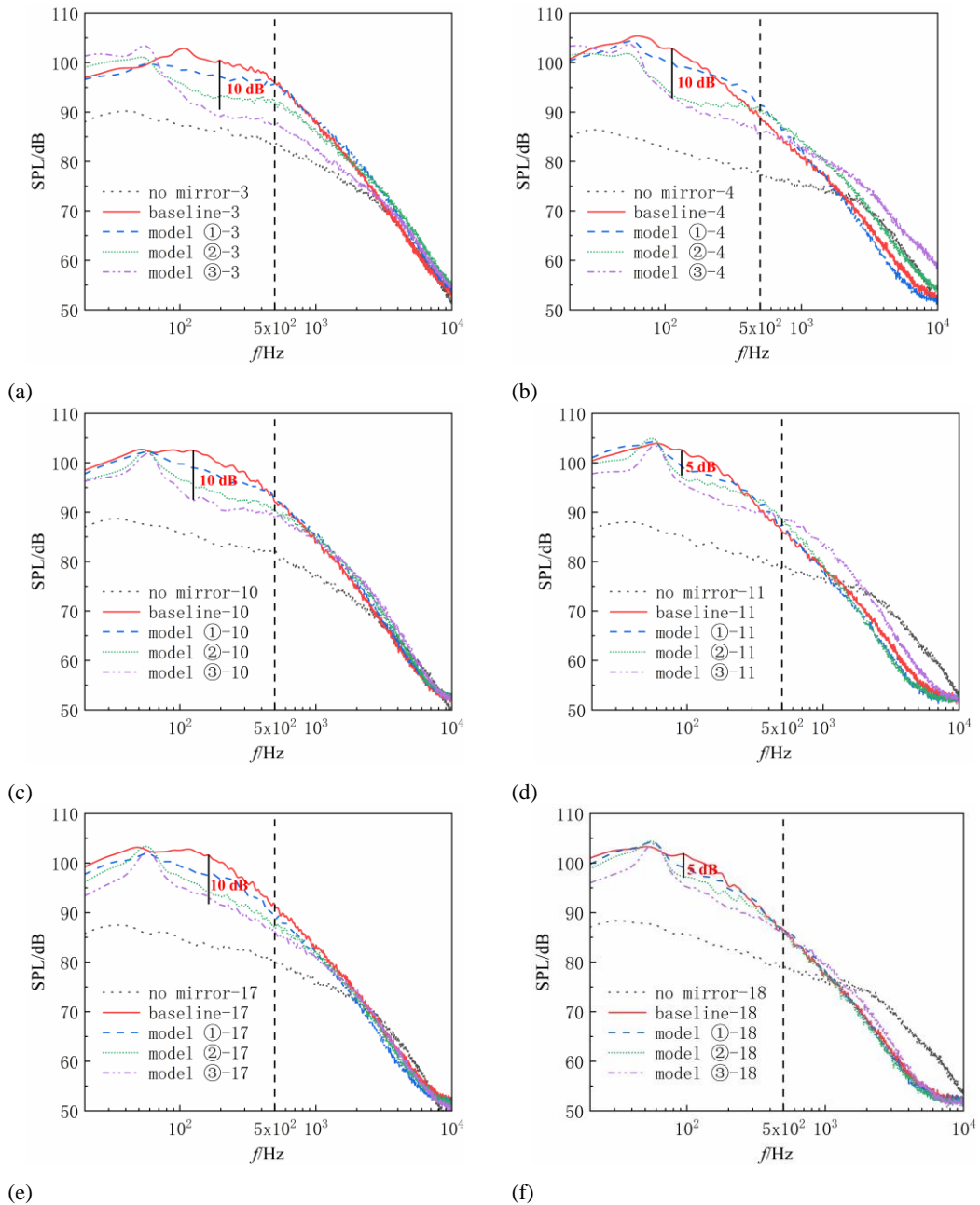The wall pulsation pressure generated by the vortices is a significant cause of aerodynamic noise.

Fig. 8. Spectrum comparison between different measuring points in the core area of the side-view mirror wake. (a) point 3; (b) point 4; (c) point 10; (d) point 11; (e) point 17; (f) point 18.

Therefore, PIV experiments were conducted on the three different sections of the side-view mirror to reveal the noise generation mechanism. Figure 9 depicts a comparison diagram of the mean streamlines on the vertical plane A for the four side-view mirrors. The color legend shows the mean streamwise x-velocity U between -15 m/s and 35 m/s. It can be seen that there are two large-scale vortex clusters in opposite directions behind all four models. Compared with the baseline, the vortex clusters behind the three slotted models move away from the wall surface, mainly due to the air flowing through the slot. The average velocity of the lower part near the wall is significantly larger than that of the baseline, which is conducive to reducing the backflow.

Table 1 Average OASPL reduction in different frequency ranges at the nine measuring points

-	OASPL reduction	
	20 Hz ~ 500 Hz	20 Hz~ 10 kHz
$\Delta Lp_①$ (Model ①-Baseline)	-1.8 dB	-1.5 dB
$\Delta Lp_②$ (Model ②-Baseline)	-3.9 dB	-3.3 dB
$\Delta Lp_③$ (Model ③-Baseline)	-5.1dB	-4.6 dB

Fig. 9. Comparison of mean streamlines of different side-view mirrors at plane A: (a) baseline; (b) model ①; (c) model ②; (d) model ③.
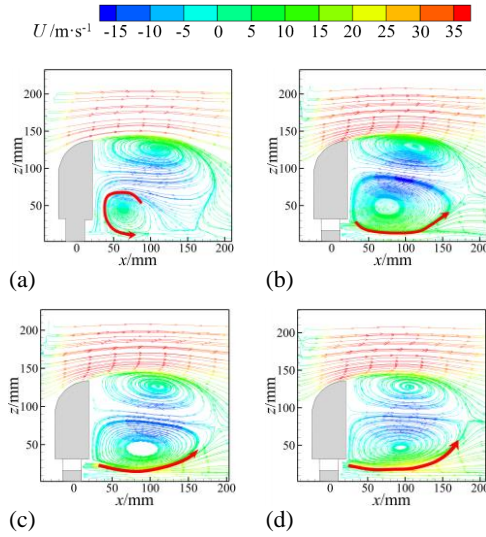

Fig. 11. Comparison of mean streamlines of different side-view mirrors at plane C: (a) baseline; (b) model ①; (c) model ②; (d) model ③.

The corresponding mean streamlines on horizontal plane B are presented in Fig. 10. There is a blind area without streamlines due to the lack of laser light. We can notice that the size and structure of the two vortex clusters behind all models are very similar, indicating that the slot in the base foot has little effect on the upper wake flow of the mirror housing.
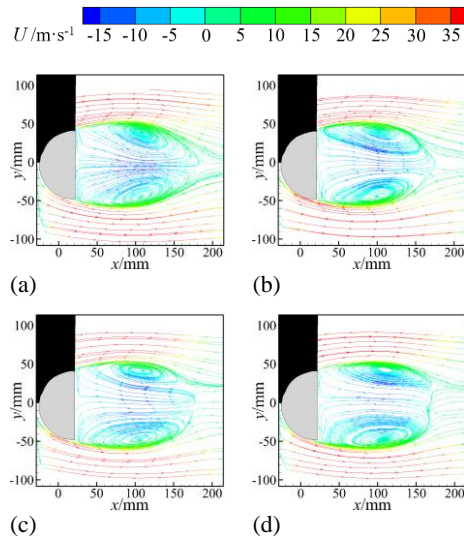

Fig. 10. Comparison of mean streamlines of different side-view mirrors at plane B: (a) baseline; (b) model ①; (c) model ②; (d) model ③.

Figure 11 presents the mean streamlines of four models on horizontal plane C. There is a big difference between the slotted mirror and the baseline mirror in this area close to the plate wall
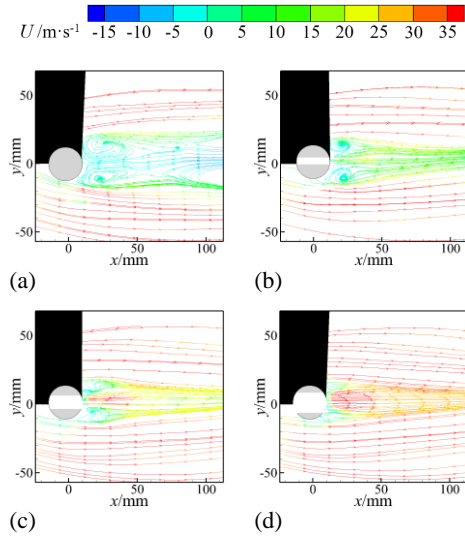
surface. Two large-scale vortex clusters are formed behind the baseline, and the backflow region exists in the whole PIV shooting area. However, as the slotting rate increases, both the size of the vortex clusters and the backflow area behind the model gradually decrease. When the slotting rate reaches 30%, the vortex clusters and the backflow area almost disappear.

3.3 Turbulence intensity

Since the flow field characteristics at planes A and C can better reveal the influence of wake on the pressure fluctuation of the side window, the turbulent kinetic energies (TKE) at these two planes were compared and analyzed below. The TKE is defined by

$$\text{TKE} = (\tilde{u}_x^2 + \tilde{u}_y^2 + \tilde{u}_z^2)/2 \qquad (2)$$

where $\tilde{u}_x, \tilde{u}_y, \tilde{u}_z$ are the x-streamwise, y-direction and z-direction fluctuating velocities, respectively. Due to the 2D PIV data, one of the fluctuating velocities was substituted by the other two velocities. Based on the assumption of flow isotropy, for the velocity on plane A, $\tilde{u}_y^2 = (\tilde{u}_x^2 + \tilde{u}_z^2)/2$, therefore, the TKE was calculated by the following

$$\text{TKE} = 3(\tilde{u}_x^2 + \tilde{u}_z^2)/4. \qquad (3)$$

and for plane C, $\tilde{u}_z^2 = (\tilde{u}_x^2 + \tilde{u}_y^2)/2$, and TKE $= 3(\tilde{u}_x^2 + \tilde{u}_y^2)/4$.

Figure 12 shows the comparison of the TKE of the four models at plane A, and Fig. 13 presents the comparison at plane C. The measurement of the TKE is a method used to describe turbulent motion. The higher the TKE is, the greater the turbulence, and the stronger the pressure fluctuation it generates, resulting in higher aerodynamic noise (Ye *et al.* 2021).

In Fig.12, the red dotted line indicates the flow area close to the plate wall surface. Compared with the baseline mirror, the TKE of each slotted mirror in the region close to the wall is smaller, although there is not much difference in the other areas. With the slot airflow rate increasing to $S_r =20\%$ or above (models ② and ③), the turbulence intensity near the all is significantly reduced, resulting in the reduction of the pressure fluctuation on the wall surface, as indicated in Fig. 8. This reduction of TKE behind the mirror foot is also reflected in Fig.13, where the strong turbulence existing in the core center of the baseline mirror wake has been significantly suppressed when the slot airflow rate S_r reaches 30% (model ③). At the other two airflow rates (10% and 20%), however, the turbulence in the core area at Plane C has not much different from the baseline mirror. These changes in turbulent kinetic energy behind the three slotted models contribute to the wall pressure fluctuation reduction.

3.4 Proper Orthogonal Decomposition (POD) Modes

The velocity field snapshots obtained by PIV were analyzed using the proper orthogonal decomposition (POD) approach to reveal further the noise reduction mechanism of the three slotted models. The POD technique is a popular tool extensively applied to identify the coherent structures in turbulent flows. Through the POD analysis, the energy structure of the flow field and the corresponding energy ratio of each POD mode can be obtained (Taira *et al.* 2017 and references included). Here, we perform the snapshot POD method to extract the most energetic coherent structures in the wake of the mirrors by computing a modal basis from the 400 captured PIV flow field snapshots. Figure 14 shows the percentage of kinetic energy held by the first 20 POD modes at plane C for the four mirrors. With increasing POD mode number, the kinetic energies for the first several modes are rapidly reduced and gradually decreases for the other higher ones. The energy changes of the first POD mode for the mirror models are significant difference on plane C, where the energy ratio of the first POD mode for the baseline reaches 29.5%, much more than the energy ratios of 12.1%, 11.7%, and 12.3% corresponding to mirror models ①, ②, and ③. Since the flow field on plane C is close to the wall plate surface, the reduction in the energy indicates that the large-scale vortices corresponding to the lower POD modes may have been reduced by the slotted foot.

Figure 15 shows the relative energy accumulation curves of the first 20 POD modes on plane C. From this, we can observe that the kinetic energy of the baseline mirror reaches 68.6%, much higher than 45.5% for model ①, 44.1% for model ②, and 40.9% for model ③. In the POD modal analysis, the lower modes with higher energy correspond to the larger-scale vortex structures. Therefore, the mirror with the slotted foot can change the large-scale vortices to small ones, and the total energy of wall pressure fluctuation on the side window is

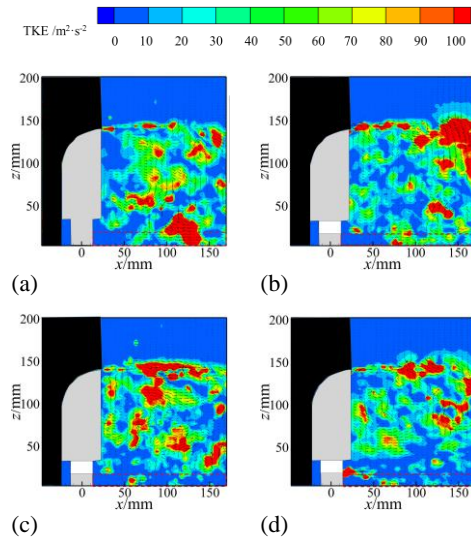weakened, effectively reducing the aerodynamic noise.

Fig. 12. Comparison of the TKE at plane A for different models: (a) baseline; (b) model ①; (c) model ②; (d) model ③.
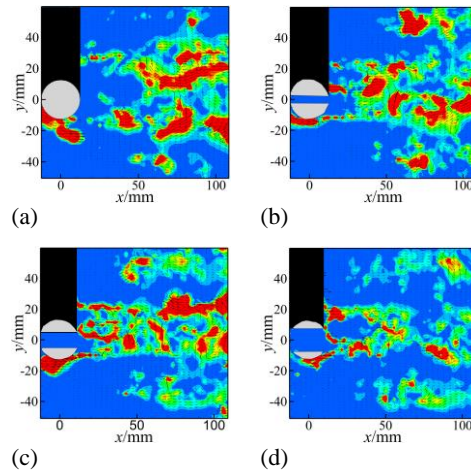

Fig. 13. Comparison of the TKE at plane C for different models: (a) baseline; (b) model ①; (c) model ②; (d) model ③.
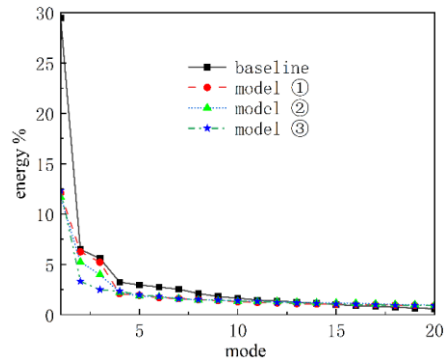

Fig. 14. Percentage of kinetic energy held by the first 20 POD modes on plane C for different mirror models.
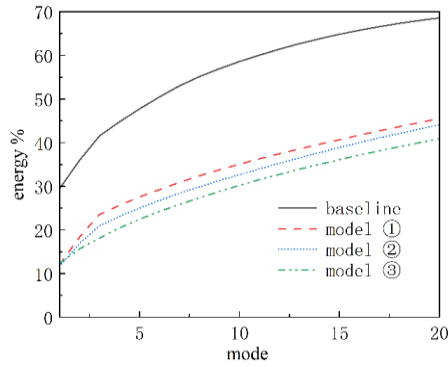
Fig. 15. Accumulation of kinetic energy held by the first 20 POD modes on plane C for different models.

Figure 16 compares the first POD mode associated with the vertical fluctuating (*v* component) velocity at plane A for four mirror models. For the baseline mirror, the structure of the first mode in the wake flow is dispersed, indicating that there has no periodic shedding of large-scale vortices. For mirror models ① and ②, we can observe a visible regular POD first mode in the wake flow, indicating that models ① and ② may have quasi-periodic large-scale vortex shedding behind the mirror. The large-scale structure corresponding to the first mode for model ③ is not apparent.
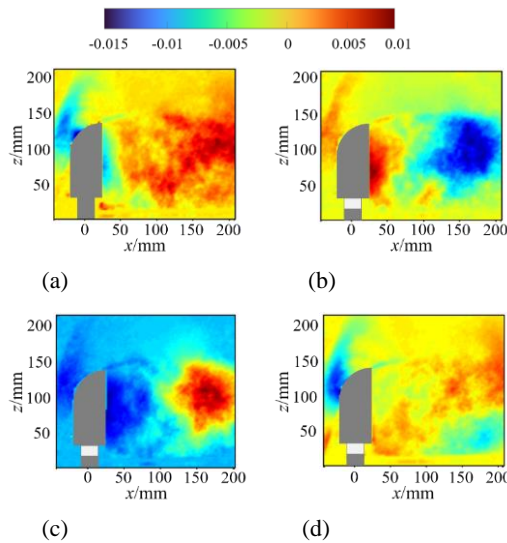

Fig. 16. First POD mode (mode-1) associated with the vertical fluctuating for flows over different models at plane A: (a) baseline; (b) model ①; (c) model ②; (d) model ③.

Figure 17 shows the second POD mode at plane A for the mirrors. We may notice that mirror model ③ has a regular POD mode in the wake flow. The POD energy distribution for the other three models is relatively diffuse. The quasi-periodic large-scale vortices behind the mirror wake will interact with the plate wall surface and produce a distinct hump at a particular frequency in its wall pressure fluctuation spectrum.
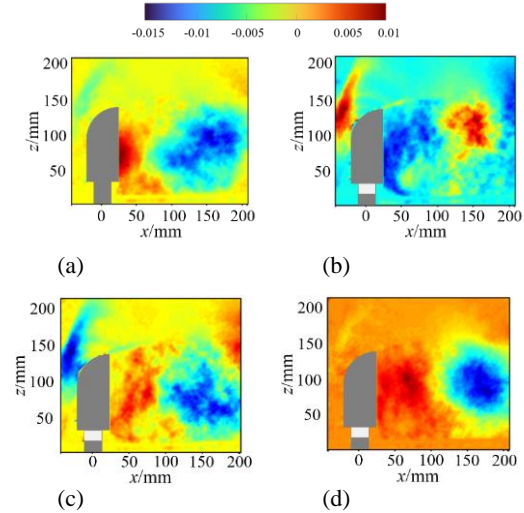

Fig. 17. The second POD mode (mode-2) associated with the vertical fluctuating for flows over different models at plane A: (a) baseline; (b) model ①; (c) model ②; (d) model ③.

3.5 Drag Coefficient

The test results of the six-component balance for the aerodynamic drag of four models are given in Table 2. Each model is tested continuously five times under the same conditions, and the average is considered the drag force of the model. The relative error δ of each test is calculated as

$$\delta = \frac{|F_n - F|}{F} \times 100\% \qquad (4)$$

where F is the average drag force of five tests for different models, and F_n is drag force of each test.

By analyzing the data in Table 2, we can see that the maximum relative errors between the five test data of each model and its average are 0.77%, 1.92%, 1.23%, and 1.31%, respectively, all of which are less than 2%, which can effectively prove the rationality of the data in this group.

Table 2 Average drag force (*F*, unit: N) of different mirror models

Test times	Average drag force F(N)			
	Baseline	Model ①	Model ②	Model ③
1	4.23	3.98	3.94	3.68
2	4.26	4.03	3.97	3.71
3	4.26	4.06	3.99	3.73
4	4.28	4.10	4.01	3.76
5	4.29	4.12	4.04	3.78
Average	4.26	4.06	3.99	3.73

The drag coefficient C_D is defined as

$$C_D = \frac{F}{\frac{1}{2}\rho U_\infty^2 S} \qquad (5)$$

where ρ is the air density taken at room temperature, U_∞ is the inlet velocity with 33.3 m/s, and S is the windward area of the side-view mirrors.

Figure 18 presents the drag coefficients of the four mirror models. We can see that the drag coefficient of the baseline mirror is reduced effectively when the cylindrical foot adopts the slot. In addition, the reduction rate increases with the slotting airflow rate increasing. When the airflow rate is 10%, 20%, and 30%, the corresponding drag coefficient is reduced by 4.1 %, 5.0 %, and 10.2 %, respectively.
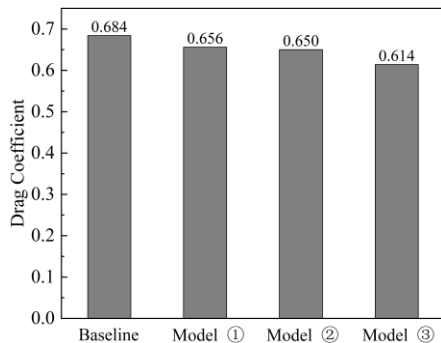

Fig. 18. Drag coefficient of different mirrors.

4. CONCLUSION AND REMARKS

To find a way to reduce the aerodynamic noise and drag force caused by automobile side-view mirrors, a generic side-view mirror consisting of a mirror housing and its cylindrical solid foot was used as the reference model. Wind tunnel experiments were carried out to investigate the flow control performance of a slotted mirror foot on the wake wall pressure fluctuation and drag force on the side-view mirror. Three airflow rates of the slotted foot, i.e., 10%, 20%, and 30%, are tested by wall pressure sensors, PIV technique, and dynamic balance. By analyzing the experimental results of the different mirror models, we draw the following conclusions:

(1) When the side-view mirror foot is slotted, the wake vortices near the wall are blown away from the surface. The turbulent kinetic energy decreases with the airflow rate increasing. On the one hand, these changes in the flow field reduce the surface pressure fluctuations on the side window, resulting in aerodynamic noise reduction of the side-view mirror. On the other hand, the airflow passing through the mirror foot reduces the aerodynamic drag force of the side-view mirror

(2) Most pressure fluctuation energies are concentrated in the low-mid frequency range. Compared to the reference mirror, the average pressure spectra at the measuring points located in the wake core area of the mirror with a slotted foot are reduced by 1.8 dB, 3.9 dB, and 5.1 dB in the range of 20 Hz~500 Hz, respectively. The corresponding drag coefficients are reduced by

4.1%, 5.0%, and 10.2% when the airflow rate from the slot reaches 10%, 20%, and 30%.

This study with respect to automotive applications concerns the incident flow uniform, while in reality, the oncoming flow in this region is intrinsically three-dimensional and potentially unsteady. Therefore, in future work, we are going to confirm the present conclusions for this simplified case with additional studies closer to the complexity of the real side-view mirror flow.

REFERENCES

Caro, S., F. G. Mendonca, V. Cotoni, P. J. Shorter and T. Connelly (2014, June). Predicting the noise transmission through a structure loaded with a low Mach number turbulent flow. In *20th AIAA/CEAS Aeroacoustics Conference*, Atlanta, American.

Chen, K. H., J. Johnson, U. Dietschi and B. Khalighi (2009). Wind noise measurements for automotive mirrors. *SAE International Journal of Passenger Cars - Mechanical Systems* 2(1), 419-433.

Chen, X., S. Wang, Y. Q. Wu, Y. Y. Li and H. Y. Wang (2018). Experimental and numerical investigations of the aerodynamic noise reduction of automotive side view mirrors. *Journal of Hydrodynamics* 30(4), 642-650.

Chen, X., W. Zhang, Y. Q. Wu, H. Y. Wang and H. Y. Ning (2014, August). Comparison and analysis on the impact of two typical rearview mirrors on aerodynamic performance. In *3rd International Conference on Energy Materials and Material Application*, Wuhan, China.

Chode, K. K., H. Viswanathan and K. Chow (2021). Noise emitted from a generic side-view mirror with different aspect ratios and inclinations. *Physics of Fluids* 33(8), 084105.

Dawi, A. H. and R. A. Akkermans (2019). Direct noise computation of a generic vehicle model using a finite volume method. *Computers & Fluids* 191, 104243.

He, Y. Z., S. Schroder, Z. H. Shi, R. Blumrich, Z. G. Yang and J. Wiedemann (2020). Wind noise source filtering and transmission study through a side glass of DrivAer model. *Applied Acoustics* 160, 107161.

Hold, R., A. Brenneis, A. Eberle, V. Schwarz and R. Siegert (1999, May). Numerical simulation of aeroacoustic sound generated by generic bodies placed on a plate: Part I - Prediction of

aeroacoustic sources. *In 5th AIAA/CEAS Aeroacoustics Conference and Exhibit*, Bellevue, WA, United states.

Hu, B. F., Z. J. Lu, Q. M. Cui, R. J. Tang, Z. Feng and D. K. Bi (2020). Prediction and aerodynamic analysis of interior noise and wind drag generated by the outside rear-view mirror for commercial vehicles. *Shock and Vibration*, 2020, 8893959.

Kato, Y. (2012). Numerical simulations of aeroacoustic fields around automobile rear-view mirrors. *SAE International Journal of Passenger Cars-Mechanical Systems* 5(1), 567-579.

Khalighi, B., K. H. Chen, J. P. Johnson, A. Snegirev, J. Shinder and S. Lupuleac (2013). Computational and experimental investigation of the unsteady flow structures around automotive outside rear-view mirrors. *International Journal of Automotive Technology* 14(1), 143-150.

Khalighi, B., A. Snegirev, J. Shinder, S. Lupuleac and K. H. Chen (2012). Simulations of flow and noise generated by automobile outside rear-view mirrors. *International Journal of Aeroacoustics* 11(1), 137-156.

Kim, D., M. Kim, E. Saredi, F. Scarano and K. C. Kim (2020). Robotic PTV study of the flow around automotive side-view mirror models. *Experimental Thermal and Fluid Science* 119, 110202.

Kim, D., A. Safdari and K. C. Kim (2021). Sound pressure level spectrum analysis by combination of 4D PTV and ANFIS method around automotive side-view mirror models. *Scientific Reports* 11(1), 1-15.

Kim, J. H. and Y. O. Han (2011). Experimental investigation of wake structure around an external rear view mirror of a passenger car. *Journal of Wind Engineering and Industrial Aerodynamics* 99(12), 1197-1206.

Kim, J. H., B. H. Park and Y. O. Han (2011). Surface flow and wake characteristics of automotive external rear-view mirror. *Proceedings of the Institution of Mechanical Engineers, Part D: Journal of Automobile Engineering* 225(12), 1605-1613.

Levy, B. and P. Brancher (2013). Topology and dynamics of the A-pillar vortex. *Physics of Fluids* 25(3), 037102.

Levy, B. and P. Brancher (2015). Experimental investigation of the wall dynamics of the A-pillar vortex flow. *Journal of Fluids and Structures* 55, 540-545.

Li, Q. L., Z. G. Yang, Y. G. Wang and Y. Z. He (2011). Experimental and numerical studies on aerodynamic noise of automotive rear view mirror. *Noise Control Engineering Journal* 59(6), 613-621.

Li, Y., Z. W. Chen and X. N. Wang (2020),

Flow/noise control of a rod-airfoil configuration using natural rod-base blowing: numerical experiments, *European Journal of Mechanics /B Fluids* 83, 99-113.

Lin, X., Y. Wang, Z. Chen, G. Dong and Z. Gu (2010). The flow and aerodynamic noise calculation of a generic side mirror. In *2010 IEEE 11th International Conference on Computer-Aided Industrial Design & Conceptual Design 1*.

Liu, Y. Y., Y. Q. Li and Z. Y. Ding (2018). Numerical simulation on the impact of the bionic structure on aerodynamic noises of side-window regions in vehicles. *Journal of Vibroengineering* 20(2), 1257-1271.

Murad, N., J Naser, F. Alam and S. Watkins (2013). Computational fluid dynamics study of vehicle A-pillar aero-acoustics. *Applied Acoustics* 74(6), 882-896.

Niu, X. F., H. J. Chen, Y. Li, X. Y. Jia, Y. W. Zhang, X. Yong and C. Li (2022) Design and performance of a small-scale acoustic wind tunnel at Wenzhou University for aerodynamic noise studies, *Applied Acoustic* 199, 109010.

Oettle, N. and D. Sims-Williams (2017). Automotive aeroacoustics: An overview. *Proceedings of the Institution of Mechanical Engineers Part D-Journal of Automobile Engineering* 231(9), 1177-1189.

Porteous, R., D. J. Moreau and C. J. Doolan (2019). The effect of the incoming boundary layer thickness on the aeroacoustics of finite wall-mounted square cylinders. *Journal of Acoustical Society of America* 146, 1808.

Siegert, R., V. Schwarz and J. Reichenberger (1999, May). Numerical simulation of aeroacoustic sound generated by generic bodies placed on a plate: Part II - Prediction of radiated sound pressure. In *5th AIAA/CEAS Aeroacoustics Conference and Exhibit*, WA, United states.

Taira, K., S. L. Brunton, S. T. Dawson, C. W. Rowley, T. Colonius, B. J. McKeon, O. T. Schmidt, S. Gordeyev, V. Theofilis and L. S. Ukeiley (2017). Modal analysis of fluid flows: An overview. *AIAA Journal* 55(12), 4013-4041.

Tomac, M. N., K. Yugulis, J. W. Gregory, J. Loftus and T. Ferrito (2011). Investigation of vibration phenomena induced by air flow over side view mirror. *Journal of Fluids Engineering* 133(12), 121102.

Walker, R. and W. Wei (2007). Optimization of mirror angle for front window buffeting and wind noise using experimental methods. *SAE Technical Paper*, 2007-01-2401.

Wan, J. and L. Ma (2017). Numerical investigation and experimental test on aerodynamic noises of the bionic rear view mirror in vehicles. *Journal of Vibroengineering* 19(6), 4799-4815.

Wang, Y. P., Z. Q. Gu, W. P. Li and X. H. Lin

(2010). Evaluation of aerodynamic noise generation by a generic side mirror. *World Academy of Science, Engineering and Technology* 61, 364-371.

Yang, Z. D., Z. Q. Gu, J. Y. Tu, G. P. Dong and Y. P. Wang (2014). Numerical analysis and passive control of a car side window buffeting noise based on Scale-Adaptive Simulation. *Applied Acoustics* 79, 23-34.

Yao, H., L. Davidson and Z. Chroneer (2018). Investigation of interior noise from generic side-view mirror using incompressible and compressible solvers of DES and LES. *SAE Technical Paper* 2018-01-0735.

Ye, J., M. Xu, P. Xing, Y. Cheng, D. X. Meng, Y. L. Tang and M. T. Zhu (2021). Investigation of aerodynamic noise reduction of exterior side view mirror based on bionic shark fin structure. *Applied Acoustics* 182, 108188.

Zheng, Z. Y. and R. X. Li (2012). Analysis of the automobile's external aerodynamic noise field characteristics based on CAA. In *Applied Mechanics and Materials*, Trans Tech Publ Ltd.

Zhu, J. J. and G. W. Liu (2018). Numerical optimization for aerodynamic noises of rear view mirrors of vehicles based on rectangular cavity structures. *Journal of Vibroengineering* 20(2), 1240-1256.